XMM-Newton observations of the giant H II region N 11 in the LMC[*]

Y. Nazé[**,1], I.I. Antokhin[***,1,2], G. Rauw[†1], Y.-H. Chu[3], E. Gosset[†1], and J.-M. Vreux[1]

[1] Institut d'Astrophysique et de Géophysique; Université de Liège; Allée du 6 Août 17, Bat. B5c; B 4000 - Liège; Belgium
[2] Astronomy and Astrophysics Group; Department of Physics and Astronomy; Kelvin Building, University of Glasgow; Glasgow G12 8QQ; United Kingdom
[3] Astronomy Department; University of Illinois at Urbana-Champaign; 1002 West Green Street; Urbana, IL 61801; USA

Abstract. Using the sensitive *XMM-Newton* observatory, we have observed the giant H II region N 11 in the LMC for ~30 ks. We have detected several large areas of soft diffuse X-ray emission along with 37 point sources. One of the most interesting results is the possible association of a faint X-ray source with BSDL 188, a small extended object of uncertain nature.
The OB associations in the field-of-view (LH9, LH10 and LH13) are all detected with *XMM-Newton*, but they appear very different from one another. The diffuse soft X-ray emission associated with LH9 peaks near HD 32228, a dense cluster of massive stars. The combined emission of all individual massive stars of LH9 and of the superbubble they have created is not sufficient to explain the high level of emission observed: hidden SNRs, colliding-wind binaries and the numerous pre-main sequence stars of the cluster are most likely the cause of this discrepancy. The superbubble may also be leaking some hot gas in the ISM since faint, soft emission can be observed to the south of the cluster. The X-ray emission from LH10 consists of three pointlike sources and a soft extended emission of low intensity. The two brightest point sources are clearly associated with the fastest expanding bubbles blown by hot stars in the SW part of the cluster. The total X-ray emission from LH10 is rather soft, although it presents a higher temperature than the other soft emissions of the field. The discrepancy between the combined emission of the stars and the observed luminosity is here less severe than for LH9 and could be explained in terms of hot gas filling the wind-blown bubbles. On the other hand, the case of LH13 is different: it does not harbour any extended emission and its X-ray emission could most probably be explained by the Sk −66°41 cluster alone.
Finally, our *XMM-Newton* observation included simultaneous observations with the OM camera that provide us with unique UV photometry of more than 6000 sources and enable the discovery of the UV emission from the SNR N11L.

Key words. ISM: individual objects: LMC N11 – Magellanic Clouds – Galaxies: star clusters – Ultraviolet: stars – X-rays: general

1. Introduction

Massive stars are known to deeply influence the structure and dynamics of their environment. Their fast stellar winds combined with their huge mass-loss rates and their powerful explosion as supernovae (SNe) can shape the interstellar medium (ISM), creating various structures from small wind-blown bubbles around single stars to large superbubbles around OB associations. This collective action can best be understood by studying nearby H II regions, with embedded OB associations containing hundreds of massive stars. In this context, we have chosen to study the N 11 complex (Henize 1956) in the Large Magellanic Cloud (LMC).

N 11 is the second largest H II region in the LMC after 30 Doradus, and it may constitute a more evolved version of this latter nebula (Walborn & Parker 1992). It harbors several associations of massive stars: LH9, LH10, LH13 and LH14 (Lucke & Hodge 1970). Its structure is complex and reflects the interactions between the stars and their environment. The central cluster, LH9, is surrounded by a filamentary shell of ~120 pc in diameter. The combined action of stellar winds and supernova explosions from the members of the cluster has carved a hollow cavity in the surrounding ISM, thereby creating the shell which is also called a superbubble. The hot shocked winds/ejecta that fill this cavity emit X-rays (Mac Low et al. 1998) and provide the pressure to drive the superbubble shell expansion. Only supernovae outside the superbubble can produce distinct supernova remnants (SNRs) such as N11L at the western edge of the N11 complex (Williams et al. 1999).
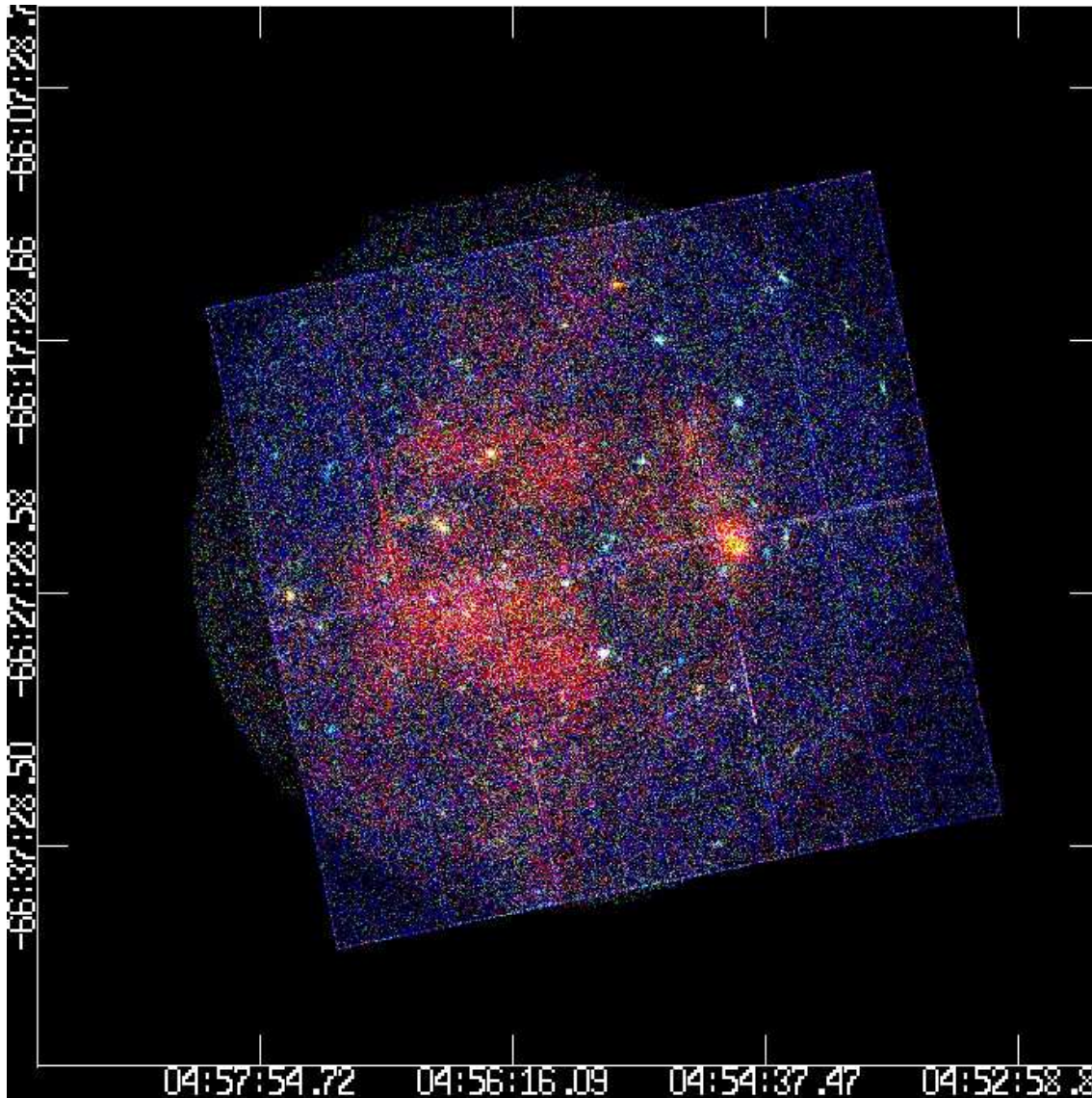
Fig. 1. Three colour image of the N 11 region as seen by the combined EPIC cameras. The red, green and blue colours correspond respectively to the $0.4 - 1.0$ keV, $1.0 - 2.0$ keV and $2.0 - 10.0$ keV energy bands. Note that this image is based on a pn event list that was filtered using #XMMEA_EP and $0 \leq$ pattern ≤ 12. This event list was only used for aesthetic reasons in the aim of creating Figs. 1 & 2, not for any scientific analysis.

The action of LH9 on its surroundings has also triggered a burst of star formation at the periphery (Rosado et al. 1996), leading to the birth of the three other OB associations. Situated to the north of LH9, LH10 is still embedded in its natal cloud but its most massive components have already begun to blow bubbles around them (Nazé et al. 2001). The stellar population of LH9 and LH10 has been studied by Parker et al. (1992, hereafter PGMW) and Walborn et al. (1999). To the east of LH9 lies LH13, which appears to contain two tight clusters, Sk $-66°41$ and HNT (Heydari-Malayeri et al. 2000). However, the ages and radial velocities indicate that the ≤ 5 Myr old cluster Sk $-66°41$ is associated with the surrounding H ɪɪ region and the ~100 Myr old cluster HNT is unrelated and most probably just a line-of-sight object (Heydari-Malayeri et al. 2000). Situated at the northeast outskirts of N 11, LH14 is the least

studied of the four OB associations; the existence of a few massive stars in LH14 has been illustrated in a photometric study by Heydari-Malayeri et al. (1987).

In summary, the N 11 complex harbours a variety of phenomena associated with massive stars (e.g. bubbles and superbubbles), and even contains a SNR. All these objects should be associated with some hot gas. N 11 thus provides an interesting target for deep X-ray observations. A *ROSAT* investigation only permitted to detect some X-ray emission (Mac Low et al. 1998, Dunne et al. 2001), but the unprecedented sensitivity of *XMM-Newton* enables us to study this region in more details.

In the following sections, we will first describe the observations and the X-ray sources detected in the field. Next, we will focus on the main components of N 11: the SNR, the superbubble, LH10 and LH13. Finally, we will conclude in Section 6.
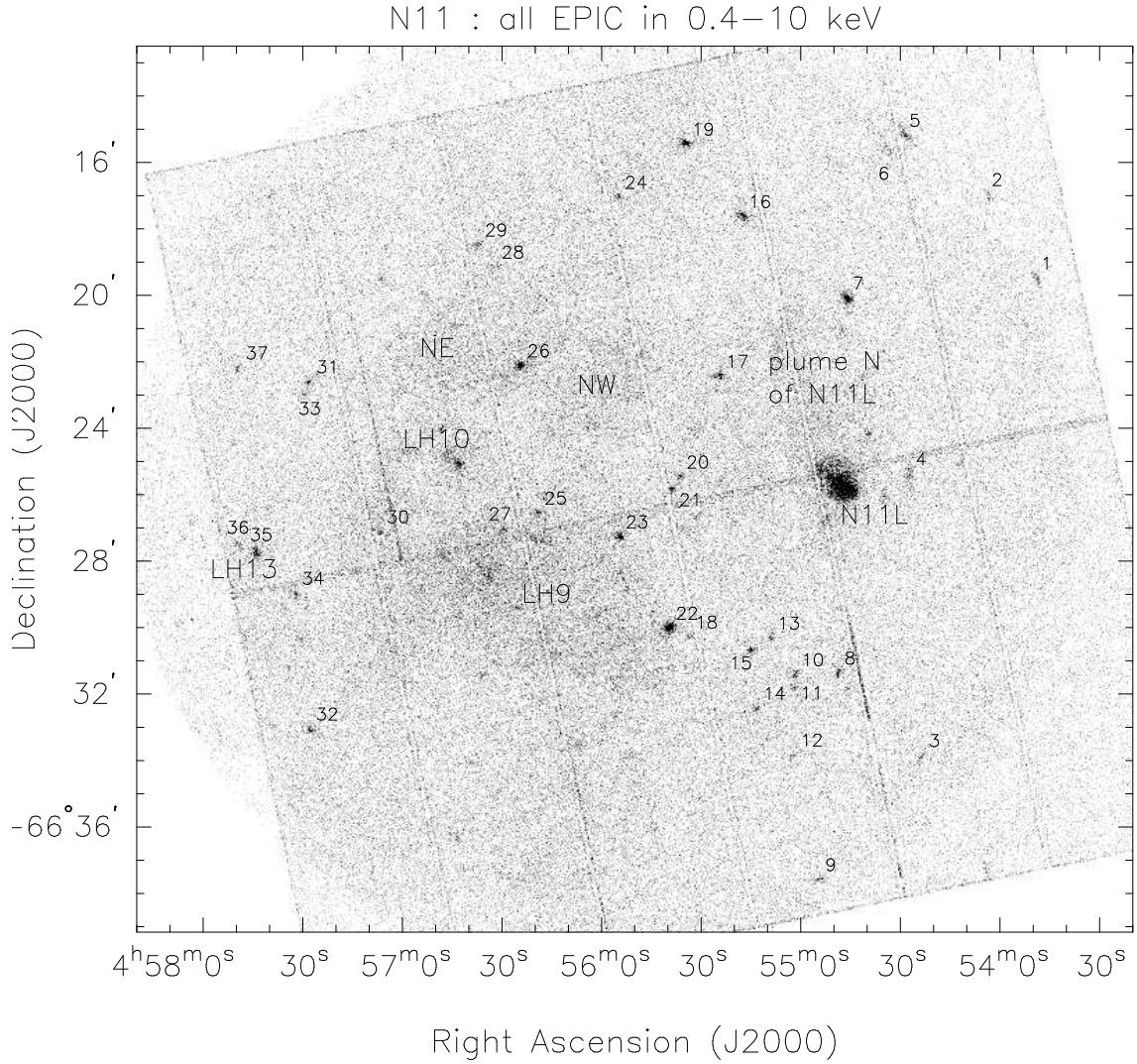
N11 : all EPIC in 0.4−10 keV

Fig. 2. Combined EPIC image of N 11 in the energy range 0.4 − 10 keV. The detected sources are labelled. The image has been binned by a factor of 50, to obtain a pixel size of 2.5″.

2. Observations

2.1. X-ray data

N 11 was observed with *XMM-Newton* (Jansen et al. 2001) in the framework of the guaranteed time of the Optical Monitor Consortium during revolution 325, on 17 Sept. 2001, for approximately 30 ks. The two EPIC MOS cameras (Turner et al. 2001) were used in full window mode, and the EPIC pn instrument (Strüder et al. 2001) was operated in extended full frame mode. A thick filter was added to reject optical light. These instruments are sensitive to radiation in the 0.4-10.0 keV range, and the on-axis spatial resolution of *XMM-Newton* is about 5″.

We used the Science Analysis System (SAS) software version 5.4.1. to reduce the EPIC data. These data were first processed through the pipeline chains, and then filtered. For EPIC MOS, only events with a pattern between 0 and 12 and passing through the #XMMEA_EM filter were considered. For EPIC pn, we kept events with flag=0 and a pattern between 0 and 4. To check for contamination by low energy protons,

we have further examined the light curve at high energies (Pulse Invariant channel number>10000, ~E>10 keV, and with pattern=0). No background flares were detected. The resulting useful exposure times are 32.5 ks, 32.5 ks, and 25.4 ks for EPIC MOS1, MOS2 and pn, respectively. Further analysis was performed using the SAS version 5.4.1. and the FTOOLS tasks. The spectra were analysed and fitted within XSPEC v11.0.1.

Figures 1 and 2 show images of the field from the combined EPIC data. Figure 1 provides a three colour image, in which numerous point sources and diffuse, soft emissions are clearly seen. Figure 2 gives the identification of the point sources detected in the field (see Sect. 3).

2.2. Optical Monitor data

During the X-ray observation, the field was also observed through two UV filters (UVW1 and UVM2) and the visible (V) filter of the Optical Monitor (OM) onboard *XMM-Newton* (Mason et al. 2001). The exposure times were 1 ks, 3 ks, and
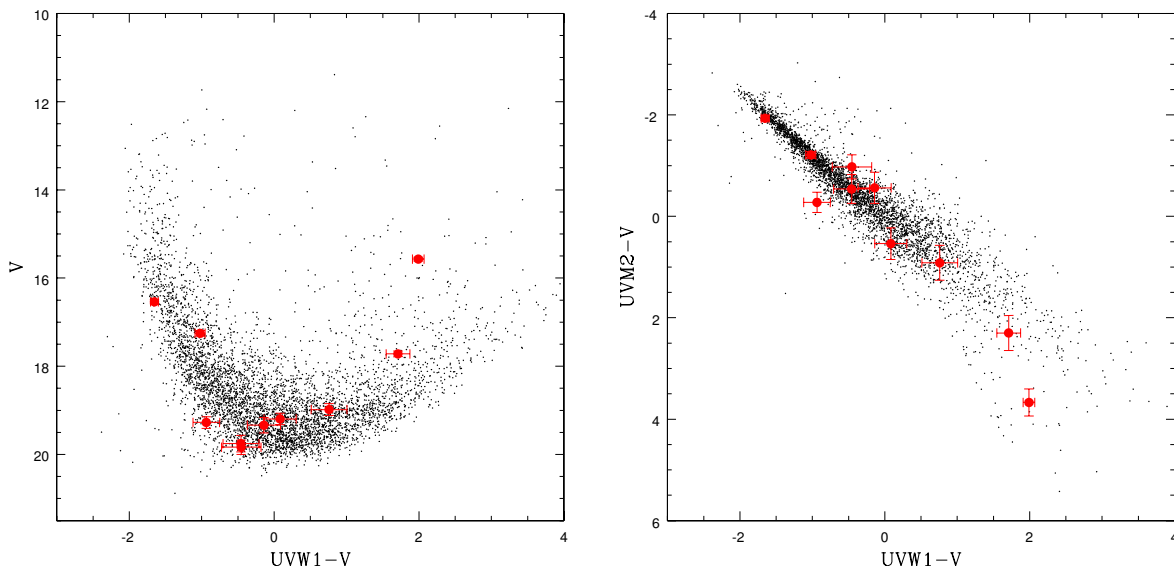
Fig. 4. Color-magnitude and color-color diagrams for all OM sources. Large dots with error bars correspond to the closest counterparts of the X-ray sources (see text).
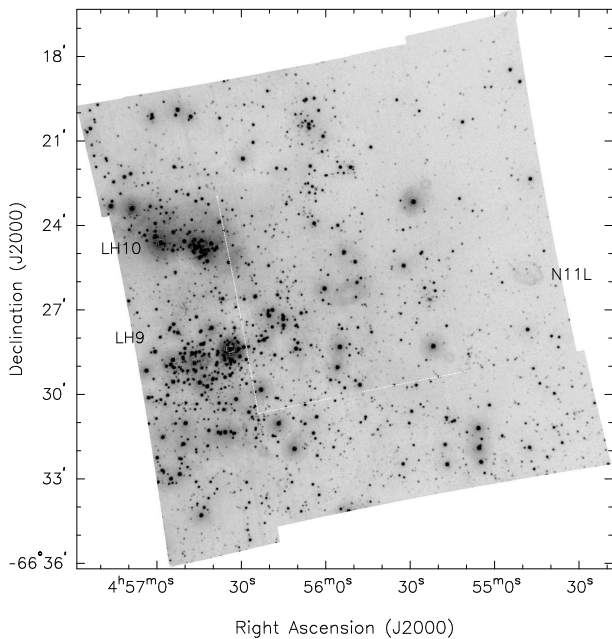

Fig. 3. Optical Monitor (OM) image of N 11 through the UV filter UVM2. Note that the FOV is smaller than the EPIC FOV. At the rightmost side of the image, the SNR N11L can be seen as a faint diffuse ring. Diffuse halos around bright stars are artefacts.

1 ks for the UVW1, UVM2, and V filters, respectively. The coverage of the full OM field necessitated five consecutive exposures. The OM is a 30 cm optical and UV telescope with extremely sensitive detectors. It is working in a photon-counting mode, analogous to the way the X-ray detectors work. The data obtained with the OM are thus quite different from the 'standard' ground-based data, and present particular features, like fixed 'modulo-8' noise and significant coincidence losses even for relatively faint objects (Mason et al. 2001). Further complications follow from the fact that the OM Point Spread Function (PSF) depends on the source brightness[1].

We used SAS tasks *omatt* and *ommosaic* to create astrometrically corrected composite images of the full field-of-view (FOV). An example of such a composite image is shown in Fig. 3 for the UVM2 filter. Note that it does not completely cover the entire EPIC FOV. A first estimate of the sky coordinates was obtained using the nominal pointing position of the telescope, and this may result in a systematic shift of our sky coordinates relative to the ideal ones by up to 4″.

Because of the particular features of the OM and of the extremely crowded nature of the field, the SAS tasks were unable to fully process the data and generate accurate photometry. For this reason, the photometric reduction was done with the daophot program in the PSF fitting mode. The sources were first detected using the *sextractor* task. The resulting list of stars was cleaned of spurious identifications, and some missing sources were added: a total of 6250 sources were then detected in this field. Next, photometry was derived for these stars using PSF-fitting. The zero point was determined by selecting relatively isolated stars and performing aperture photometry with an aperture radius of 3″. After the PSF magnitudes were adjusted to this zero point, they were scaled to the default aperture (6″) using information about the OM PSF from the SAS current calibration file OM_PSF1DRB_0006.CCF. Next, the empirical coincidence loss correction was applied and finally, instrumental V magnitudes were converted to the standard V magnitudes. These transformations are based on the

---

[1] Note that the algorithm used to derive the photometry can only handle a single PSF. However, the errors due to this approximation are certainly smaller than those due to the crowdeness of the field.

UVW1−V^{OM} color and were derived by the OM calibration team from simulations of the color transformations, using OM instrumental response curves and several spectral libraries: V = V^{OM} − 0.0165 − 0.0059 ∗ (UVW1−V^{OM}) − 0.0009 ∗ (UVW1−V^{OM})^2. In V, UVW1 and UVM2, the zero points of the OM are set to 17.9633, 17.2965 and 15.8098, respectively. The corresponding simulated magnitudes of Vega are equal to U(Vega)=0.025 mag and V(Vega)=0.03 mag (for more details about the OM calibration, see Antokhin et al., in preparation).

To get a reliable astrometric solution for the OM sources, we used the GSC 2.2 catalog. We first made a tangential projection of all GSC sources to create a linear scale approximately resembling the scale of the OM. Then, we manually cross-identified a few tens of the brighter stars from GSC and OM plots, and used the IRAF's tasks *geomap* to compute a non-linear polynomial transformation from the OM coordinate system to the GSC tangential one. Using this first approximation to cross-identify more sources, we then compute a more precise transformation (rms=0.22″), which gives reliable results for the GSC 2.2 catalog, the 2MASS All Sky Catalog of Point Sources and the USNO B1.0 catalog in the whole field. Note however that the transformation is less precise at the edges, so that we used an adaptive radius to get the actual GSC, 2MASS or USNO counterpart to the OM sources.

The OM astrometry and photometry of the >6000 sources detected in N 11 are presented in an electronic table that can be retrieved from the Centre de Données Astronomiques de Strasbourg (CDS). In this table, the first column gives the OM number of the source; the second and third columns show the OM xy coordinates; the next seven columns provide the J2000 right ascension and declination of the sources; columns 11 to 16 present the OM magnitudes in each filter, together with their error; column 17 is 'y' if the source has a 2MASS entry[2]; columns 18 to 23 yield the name and distance to the counterpart from the GSC, USNO B1.0, and PGMW catalogs, respectively.

Color-magnitude and color-color diagrams of all OM sources are shown in Fig. 4. These diagrams show a well marked main-sequence in both cases. Our V photometry is one magnitude deeper than PGMW and appears complete down to V=20 mag, which corresponds to an early A-type star on the main sequence, whereas the brightest stars rather have an O3V type. The color-magnitude diagrams of LH9, LH10, and the whole field are very similar, as was shown in classical UBV photometry by PGMW.

3. X-ray sources in the field

3.1. List of sources

The X-ray data of N 11 reveal several point sources and extended emissions, as can be seen in Fig. 1. The latter category will be extensively discussed in Sect. 4, and we will focus here only on the point sources.

To search for discrete X-ray sources, we have applied the detection metatask *edetect_chain* simultaneously to the data from the three EPIC cameras. We used three energy bands:
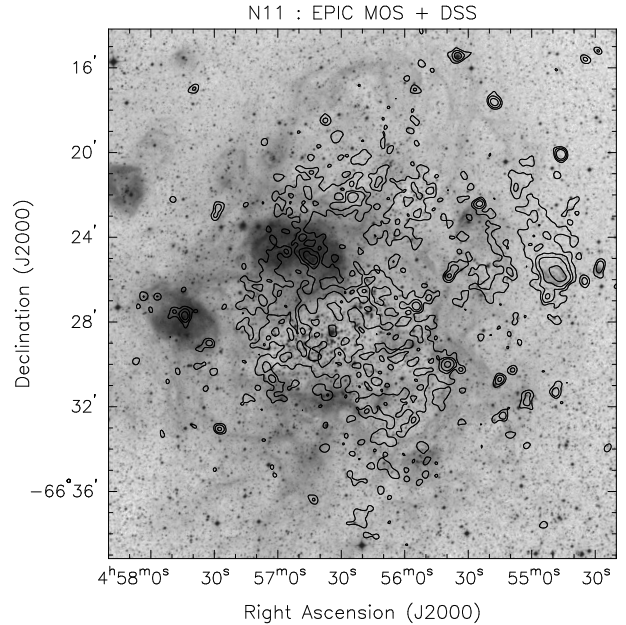

Fig. 5. X-ray contours overlaid on a DSS image of N 11. The combined X-ray data of both EPIC MOS have been binned to obtain pixels of 2.5″, and then smoothed by convolution with a gaussian (σ = 3 px). The contours are at levels 0.35, 0.5, 0.8, and 2 cts pixel^{-2}. N11B (containing LH10) is the bright nebula just northeast of the center, while N11C (LH13) and N11D (LH14) are the two easternmost nebulae of the field.

0.4 − 1.0 keV, 1.0 − 2.0 keV and 2.0 − 10.0 keV. We eliminated the false detections mainly due to structures in the diffuse emissions by rejecting the extended sources, the sources with a logarithmic likelihood < 5 in one detector and/or a combined logarithmic likelihood for the three detectors < 30. This procedure left 37 point sources in the field. Their positions are shown in Fig. 2 and their properties are presented in Table 1, in order of increasing right ascension. Their background-subtracted and vignetting-corrected count rates in each of the EPIC cameras are also indicated, together with Hardness Ratios (HRs) calculated from EPIC pn data. These HRs are defined as $HR1 = (M-S)/(M+S)$ and $HR2 = (H-M)/(H+M)$, where S, M, and H correspond to the count rates in the 0.4 − 1.0, 1.0 − 2.0 and 2.0 − 10.0 keV bands, respectively. Note that the SAS detection tasks do not apply a correction for out-of-time events or dead times. For the EPIC pn data used in extended full frame mode, this implies an overestimate of the exposure time (and thus an underestimation of the count rates) by 2.3%. Since this amount is well within the errors, we choose not to correct the pn count-rates provided by *edetect_chain*. Finally, a few sources associated with the LH10 cluster were excluded by the selection criteria defined above. They are thus not included in Table 1 but will be extensively discussed in Sect. 4.4.

3.2. Identification

We have compared our source list to the *ROSAT* detections in the same field. Six catalogs are available: Haberl & Pietsch (1999, [HP99]), Sasaki et al. (2000, [SHP2000]), the WGA cat-

---

[2] 2MASS designations are not included since they are simply the coordinates of the sources.

Table 1. Coordinates of the detected X-ray point sources with their individual count rates for each of the three detectors, in the 0.4 − 10 keV range. A missing value means the source is in a gap or out of the field-of-view for this particular detector. The Hardness Ratios (HRs) were evaluated on the EPIC pn data. The right-hand side of the table shows the results of the correlation with the GSC 2.2 catalog, the 2MASS All-Sky Catalog of Point Sources, and the USNO B1.0 catalog. In these last columns, Nr represents the number of counterparts in the correlation region, while d corresponds to the distance between the X-ray source and its counterpart, if unique.

N	Name	CR MOS1 10^{-3} cts s^{-1}	CR MOS2 10^{-3} cts s^{-1}	CR pn 10^{-3} cts s^{-1}	HR1	HR2	GSC 2.2 Nr	d(")	R	B	2MASS Nr	d(")	J	H	K	USNO B1.0 Nr	d(")	B1	R1	B2	R2	I
1	XMMU J045349.8−661928			9.9±1.6	0.44±0.14	-0.07±0.19	1	2.9		18.6	0					1	3.7			18.4	18.9	
2	XMMU J045404.6−661657			9.1±1.5	0.26±0.14	-0.41±0.25	1	3.4	17.9		0					1	2.1		17.2	18.1	16.9	17.1
3	XMMU J045423.4−663349	2.4±0.7	1.1±0.5	3.9±1.0	0.30±0.25	-0.22±0.34	1	3.4		13.8	0					1	3.8		18.5	18.1	18.6	
4	XMMU J045427.5−662522^a	2.2±0.6	1.9±0.5				0				0					2						
5	XMMU J045429.4−661510			15.6±2.2	0.32±0.14	-0.05±0.17	0				0					0						
6	XMMU J045434.2−661537	2.9±0.9		4.7±1.2	-0.12±0.29	0.35±0.28	0				0					1	2.9		18.6	20.1	18.6	
7	XMMU J045446.4−662004	5.9±0.7	7.4±0.8	16.8±1.4	0.51±0.09	0.18±0.08	1	1.0	18.2	17.9	0					4						
8	XMMU J045448.9−663120	1.7±0.5	2.3±0.5	6.5±0.9	0.27±0.18	0.14±0.14	0				0					0						
9	XMMU J045454.6−663733	2.4±0.7	1.9±0.7	7.5±1.3	0.19±0.28	0.42±0.17	0				0					1	4.1		18.4	20.5	18.2	17.7
10	XMMU J045501.8−663123	0.8±0.3	1.1±0.3	5.3±0.7	-0.27±0.12	-0.86±0.24^g	1	1.7	14.4		1	1.8	13.9	13.5	13.4	2						
11	XMMU J045502.0−663147	1.7±0.4	1.4±0.3	3.1±0.7	0.64±0.29^e	0.00±0.21	1	0.3	17.5		0					0						
12	XMMU J045502.2−663349	0.9±0.4	1.1±0.4	3.1±0.8	0.22±0.53^e	0.57±0.21	1	3.0		18.0	0					1	2.8			17.5	18.1	
13	XMMU J045509.0−663018		1.9±0.4	3.9±0.6	1.00±0.09^e	0.43±0.13	1	0.9	17.3		1	1.4	16.0	15.2	15.3	1	1.7		16.7	15.8	16.7	
14	XMMU J045513.4−663225	1.9±0.4	1.4±0.3	3.6±0.7	0.52±0.38^e	0.43±0.16	0				0					1	4.2		17.4	15.7	17.8	
15	XMMU J045515.1−663039	2.2±0.5	3.4±0.9	4.6±0.7	0.77±0.21^e	0.08±0.14	0				0					0						
16	XMMU J045517.8−661736	3.5±0.6	4.6±0.7	8.6±1.0	0.45±0.14	0.01±0.13	0				0					0						
17	XMMU J045524.6−662224	1.7±0.3	2.3±0.3	4.7±0.7	0.77±0.16	-0.23±0.14	0				0					0						
18	XMMU J045533.8−663015	0.7±0.2	0.6±0.2	1.4±0.4		0.89±0.21^{e,f}	0				0					0						
19	XMMU J045534.9−661525^b	3.2±0.5	4.8±0.7	12.6±1.2	-0.72±0.06	-1.00±0.28^g	1	1.0		11.5	1	1.2	9.2	8.7	8.7	1	1.0	11.4	10.1	10.9	10.1	9.8
20	XMMU J045536.4−662526	0.6±0.2	1.0±0.2	2.6±0.4	1.00±0.12^e	0.21±0.16	0				0					1	4.4			20.2		17.4
21	XMMU J045538.8−662549	1.1±0.2	1.4±0.2	2.3±0.6	1.00±0.15^e	-0.05±0.26	0				0					0						
22	XMMU J045539.6−662959	5.6±0.5	5.6±0.5	17.4±1.1	0.14±0.08	-0.02±0.07	1	2.9	16.4		0					2						
23	XMMU J045554.7−662715	1.8±0.3	1.9±0.3	5.6±0.6	0.48±0.15	-0.06±0.11	0				0					0						
24	XMMU J045555.0−661701	0.9±0.3	0.9±0.4	4.4±0.8	-0.35±0.14	-0.31±0.34	0				1	0.8	15.1	14.5	14.2	0						
25	XMMU J045619.2−662631	0.9±0.2	0.9±0.3	2.0±0.5	0.46±0.39^e	0.04±0.22	0				0					0						
26	XMMU J045624.3−662205	2.8±0.4	3.0±0.4	8.0±0.8	0.06±0.12	-0.17±0.10	0				0					0						
27	XMMU J045629.7−662701^c	0.5±0.2	0.7±0.3	2.0±0.5	0.49±0.49^e	0.30±0.21	0				0					2						
28	XMMU J045632.2−661908	0.8±0.3	0.4±0.3	2.4±0.6	1.00±0.31^e	0.05±0.24	0				0					0						
29	XMMU J045637.1−661828	0.7±0.3	1.4±0.4	4.5±0.7	0.25±0.25	0.22±0.16	0				0					1	2.9		16.9	15.0		17.2
30	XMMU J045706.7−662705	0.8±0.4	1.1±0.3	3.4±0.7	0.41±0.25	-0.16±0.21	1	3.5	16.3		0					2						
31	XMMU J045727.9−662234	1.3±0.4	1.5±0.4	4.8±0.9	0.67±0.27^e	0.49±0.13	0				0					0						
32	XMMU J045728.1−663302	2.8±0.5		8.1±1.2	1.00±0.41^e	0.57±0.11	1	2.5	16.4		0					0						
33	XMMU J045729.2−662256	1.1±0.4	1.5±0.4	2.7±0.7	1.00±0.25^e	0.41±0.23	0				0					0						
34	XMMU J045732.2−662856	1.5±0.4	0.7±0.3	3.9±0.9	0.27±0.31	0.24±0.22	0				0					0						
35	XMMU J045744.1−662741^d	3.9±0.6	2.5±0.5	10.4±1.2	-0.15±0.11	-1.00±0.14^g	1	0.9		11.8	1	1.2	11.9	12.0	11.9	1	0.9	12.1	13.0	12.7	13.1	13.3
36	XMMU J045749.2−662726	1.6±0.4	0.5±0.3	3.1±1.0	0.00±0.30	0.28±0.35	0				0					0						
37	XMMU J045749.2−662210	1.4±0.4		5.1±1.0	0.56±0.26	0.28±0.17	0				0					0						

^{a}This source corresponds to BSDL 188 (see Fig. 7 and Sect. 3.5). An infrared source, IRAS 04543−6629, is situated at 4$''$1 from the X-ray source, and may be coincident with it.
^{b}This source corresponds to HD 268670 (B=11.3,V=10.49, spectral type K0).
^{c}PGMW 2088 (B=18.6, V=18.8) lies at 1$''$9 from this source.
^{d}This source corresponds to the tight cluster HD 268743 (Sk−66°41, B=11.6, V=11.7, combined spectral type O3V((f*))+OB)
^{e}For this source, the count rate in the soft band is, within the errors, close to zero.
^{f}For this source, the count rate in the medium band is, within the errors, close to zero.
^{g}For this source, the count rate in the hard band is, within the errors, close to zero.

alog (White et al. 2000, 1WGA) and three catalogs from the *ROSAT* teams (*ROSAT* consortium 2000a, 1RXH; *ROSAT* consortium 2000b, 2RXP; and Voges et al. 1999 & 2000, 1RXS). The source detection algorithms used in the last four catalogs were most probably confused by the presence of diffuse emissions and generated a lot of false detections. They should thus be taken more cautiously than the first two and are only given here for information. The cross-correlations between *XMM-Newton* and *ROSAT* source names are presented in Table 2. For completeness, the positional error on the *ROSAT* detections and their separation from the *XMM-Newton* sources are also listed in the last two columns of the Table. Generally, the sources' positions agree within the errors. There seems to be no bright transient source in the field of N 11.

To search for optical counterparts, we have cross-correlated our source list with the Simbad catalog, the USNO B1.0 catalog, the 2MASS All-Sky Catalog of Point Source and the GSC 2.2 catalog. We have defined a candidate counterpart as an object lying less than 5″ (the FWHM of the *XMM-Newton* PSF) from the X-ray source. 21 X-ray sources may possess such visible counterparts, and we give the latter in the right-hand side of Table 1, together with the separation between the X-ray sources and these objects, and some basic informations about them. Fig. 5 presents X-ray contours overlaid on a DSS image of the field. Note that the LH14 cluster is not included in the *XMM* FOV. Our 5″ criterion failed to associate XMMU J045744.1−662741 (source #35) with Sk −66°41, due to the low precision of the coordinates of this object in the catalog of Sanduleak (1970)[3]. However, as there is little doubt about this identification (see Sect. 5), it was added to Table 1. We also note that XMMU J045538.8−662549 (source #21) is quite close to a bright Cepheid (see below).

Counterparts were also identified from the OM data. Using our astrometric solution for the OM sources (see Sect. 2.2), we correlated the OM source list with the X-ray one. Table 3 gives the photometry of the OM counterpart(s) found within 5″ of our X-ray sources. The optical counterparts of the X-ray sources can be compared with field sources in the color-magnitude and color-color diagrams presented in Fig. 4. Even if the OM filter combination used in our observation is not optimal for classification purposes (see Royer et al. 2000), the colors apparently favor a stellar origin for most of these counterparts. The majority lies within the main sequence of the clusters, but the counterpart of XMMU J045501.8−663123 (source #10) is a rather bright red star lying clearly outside the main sequence. Only a very small number of these OM counterparts may possibly be quasars at low redshift, but quasars at high redshift are highly improbable.

3.3. Variability

We have analysed the lightcurves of the 6 brightest point sources (i.e. with at least 50 cts in EPIC MOS and 100 cts in EPIC pn in the $0.4 − 10.0$ keV range). The count rates in

---

[3] Note that if we use the coordinates found in the USNO, GSC, and 2MASS catalogs, the X-ray source is less than $1.''2$ away from the cluster core.

Table 2. X-ray sources previously detected in the field. The number in the first column refers to our internal numbering scheme (see Table 1). Identifications with the 2RXP and 1WGA catalogs have only an indicative value. When there were two entries with the same name in the 1WGA catalog, we kept only the source detected with the smallest off-axis angle, as recommended by the WGA team. The second part of the Table deals with the diffuse extended emissions. Several spurious X-ray sources were detected in the 2RXP and 1WGA catalogs at their position, and we will not list them here.

N	*ROSAT* name	Pos. error (″)	Sep. (″)
5	2RXP J045431.1−661530	15	22.2
6	2RXP J045431.1−661530	15	20.8
9	[HP99] 394	18.1	2.7
	2RXP J045455.2 − 663731	8	4.0
10	2RXP J045502.5−663126	8	4.2
15	2RXP J045516.1−663041	4	5.9
16	2RXP J045518.4−661738	5	3.8
17	2RXP J045523.9−662232	11	8.3
19	2RXP J045535.4 − 661522	7	4.8
	1WGA J0455.6 − 6615	13	13.5
21	1WGA J0455.6−6626	50.	35.8
22	[SHP2000] LMC14	7.7	1.4
	2RXP J045540.5 − 662958	4	5.3
	1WGA J0455.6 − 6629	13	6.1
24	2RXP J045553.6 − 661709	11	11.0
	2RXP J045555.3 − 661715	12	13.5
26	1WGA J0456.3−6622	13	7.0
35	2RXP J045744.0 − 662739	4	2.3
	2RXP J045744.9 − 662744	6	5.6
	1WGA J0457.7 − 6627	13	6.3
N11L	[SHP2000]LMC13	8.3	
	[HP99]329	4.8	
LH9	[HP99] 345	12.2	

each bin were background-subtracted using annuli around the sources or close-by circles for the background estimation regions. The effective bin lengths were calculated by taking into account the 'good time intervals' defined in Sect. 2. The resulting lightcurves were analysed using Kolmogorov-Smirnov and χ^2 tests. We also ran a modified probability of variability test (Sana et al. 2004) on the event lists of these sources. In the N 11 field, no source was found significantly variable over the time of our observation.

3.4. Spectral properties

We have also extracted[4] the spectra of these brightest sources. We have generated response matrix files (rmf) and ancillary response files (arf) using the SAS tasks *rmfgen* and *arfgen*. The spectra were binned to reach a minimum of 10 cts per channel. Finally, we analysed the background-corrected spectra within XSPEC. Due to strong noise at very low and very high energies, we have discarded bins below 0.4 keV or above 10 keV.

---

[4] To ensure a correct determination of the X-ray properties of the sources, all extractions (spectra, lightcurves) were made in detector coordinates.

Table 3. Photometry of the OM counterparts lying within 5″ from X-ray sources. The number in the first column refers to our internal numbering scheme (see Table 1).

N	V±σ_V (mag)	UVW1±σ_{UVW1} (mag)	UVM2±σ_{UVM2} (mag)	Sep. (″)
10	15.57 ± 0.04	17.56 ± 0.07	19.24 ± 0.26	1.7
11	19.34 ± 0.18	19.20 ± 0.15	18.78 ± 0.25	1.8
13	17.72 ± 0.06	19.43 ± 0.15	20.02 ± 0.34	1.0
14	19.76 ± 0.19	19.30 ± 0.16	19.22 ± 0.21	4.4
17	19.84 ± 0.17	19.38 ± 0.22	18.86 ± 0.17	2.8
	20.00 ± 0.16	19.43 ± 0.19	18.56 ± 0.18	3.7
20	17.25 ± 0.06	16.23 ± 0.03	16.04 ± 0.03	4.4
22	19.27 ± 0.13	18.34 ± 0.13	19.00 ± 0.15	0.2
27	19.20 ± 0.13	19.28 ± 0.18	19.73 ± 0.28	1.8
	19.44 ± 0.20	19.23 ± 0.19	18.89 ± 0.17	4.5
28	18.98 ± 0.13	19.74 ± 0.21	19.90 ± 0.32	3.6
30	16.54 ± 0.05	14.89 ± 0.03	14.60 ± 0.02	3.7

We have fitted the spectra with an absorbed *mekal* model or an absorbed power-law. For each source, we have fitted separately EPIC MOS1+2 and EPIC pn data, but as they gave similar results – within the errors – we finally fitted all three instruments at the same time and we list the parameters of the best-fit models in Table 4.

3.5. Individual sources

– XMMU J045427.5−662522 (source # 4):
One of the most interesting discoveries in this field is the X-ray emission associated with a small ellipsoidal object west of N 11 L, roughly 28″× 24″in size. This extended object correponds to BSDL 188, also known in Simbad as MSX LMC 1241, which is classified as an emission nebula plus association in Bica et al. (1999). But this object also correlates well with an IR source (IRAS 04543−6630, or LEDA 89996, or QDOT B0454225−662949) classified as a nearby galaxy of radial velocity ∼ 7100 − 8500 km s^{-1}(Lawrence et al. 1999, LEDA database). At that position, two extended objects are also listed in the 2MASS Extended Sources Catalog: 2MASX 04542820−6625275 (radius=29″) and 2MASX 04542184−6625310 (radius=15″). Since Bica et al. (1999) did only an imaging survey without any spectroscopic information, the BSDL 188 "nebula" probably corresponds to this galaxy. Unfortunately, it lies outside the OM field-of-view and we thus cannot provide any information on the UV emission of this object. We note however that the X-ray source is not exactly centered on the extended object, but is slightly off-axis. We also remark that the X-ray source is not extended, as far as the resolution of *XMM-Newton* can tell. Deeper investigations of this peculiar source are needed to better understand the nature of the extended object and the underlying mechanisms of the X-ray emission.

– XMMU J045446.4−662004 and XMMU J045517.8−661736 (i.e. our sources # 7 and # 16):
Their poor fit by a *mekal* model, large hardness ratios,

rather large N(H) (3−5×10^{21} cm^{-2}), and Γ ∼ 1.7 − 1.8 suggest that these sources are actually extragalactic background objects. Approximately one third of the point sources detected in this field possess large HRs, and probably do not belong to the LMC.

– XMMU J045534.9−661525 = HD 268670 (source # 19):
This low-mass foreground K0 star is clearly detected in our observation, with an X-ray flux of ∼2×10^{-14} ergs s^{-1} cm^{-2}. No significant X-ray variability was found for this source. The X-ray spectrum of this object is well fitted by an optically thin thermal plasma model but not by a power law, in agreement with the idea of this being a coronal emission from a late-type star.

– XMMU J045538.8−662549 (source # 21):
This source is 21″ away from a Cepheid star of type G2Iab. X-ray emission from Cepheids has never been detected (e.g. Evans et al. 2002), and it is not clear that the X-ray source is physically associated with the Cepheid. If it is the case, then a companion would most probably be responsible for the X-ray emission.
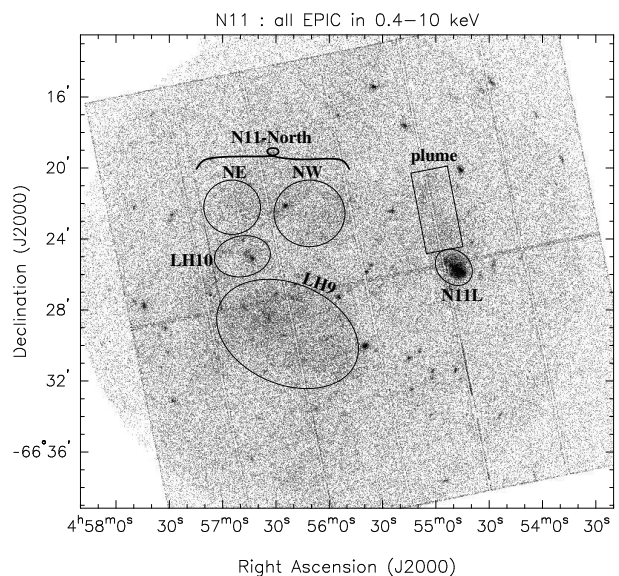

Fig. 6. Regions of extraction for each diffuse source. Circles of radius 30″ centered on point sources XMMU J045619.2−662631 (source #25), XMMU J045624.3−662205 (source #26), and XMMU J045629.7−662701 (source #27) were excluded from the extractions. The northern extended emission was cut in two parts, since it lies on two different EPIC pn CCDs.

4. Diffuse emissions

Soft diffuse emission is seen throughout the field (see Fig. 1). The brightest and most compact diffuse X-ray emission region corresponds to the SNR N11L. Extended diffuse X-ray emission covers LH9, LH10 and a region to the north of these clusters (see Figs. 5 and 6). The emission associated with N11L, LH9 and LH10 will be discussed more extensively in Sects. 4.2,

Table 4. Parameters of the spectral fits for the brightest point sources. Stated errors correspond to the 90 % confidence level. The global metallicity was set to $0.3\,Z_\odot$, as appropriate for the LMC, for all sources except XMMU J045534.9−661525 (source # 19), for which we adopt solar abundances since it corresponds to a foreground star. Absorbed fluxes are given in the spectral range $0.4 - 10$ keV and in units 10^{-14}ergs cm^{-2} s^{-1}. The results correspond to a simultaneous fit of all EPIC spectra available. A constrained fit for XMMU J045744.1−662741 is also listed below.

N	Parameters of the *mekal* model				Parameters of the absorbed power law			
	N(H) $(10^{22}$ cm$^{-2})$	kT (keV)	χ^2_ν(dof)	f_X^{abs}	N(H) $(10^{22}$ cm$^{-2})$	Γ	χ^2_ν(dof)	f_X^{abs}
7	$0.21^{0.43}_{0.07}$	$14.2^{100.}_{4.2}$	1.01 (47)	6.81	$0.33^{0.66}_{0.16}$	$1.68^{2.23}_{1.29}$	0.98 (47)	6.55
16	$0.36^{0.76}_{0.07}$	$6.40^{100.}_{2.68}$	1.50 (29)	4.33	$0.45^{1.03}_{0.20}$	$1.80^{2.69}_{1.47}$	1.49 (29)	4.57
19	$0.45^{0.66}_{0.}$	$0.24^{0.31}_{0.18}$	1.08 (41)	1.99	$1.11^{1.19}_{1.03}$	$10.^{10.}_{8.40}$	1.30 (41)	1.95
22	$0.05^{0.17}_{0.}$	$7.14^{20.7}_{4.16}$	0.82 (66)	5.93	$0.10^{0.26}_{0.02}$	$1.68^{2.02}_{1.44}$	0.84 (66)	6.28
26	$0.87^{1.24}_{0.55}$	$0.76^{1.10}_{0.57}$	0.99 (58)	1.19	$0.37^{0.64}_{0.14}$	$3.25^{4.44}_{2.69}$	1.01 (58)	1.56
35	$0.^{0.22}_{0.}$	$0.84^{1.10}_{0.73}$	1.16 (19)	1.85	$0.14^{0.36}_{0.04}$	$3.47^{4.18}_{2.79}$	0.91 (19)	2.84
35[1]	$0.06^{0.41}_{0.06}$	$0.94^{1.09}_{0.58}$	1.29 (19)	1.78				

[1] N(H) constrained to the interval $0.06 - 0.6 \times 10^{22}$ cm^{-2} (see Sect. 4.1).

Table 5. Parameters of the spectral fits for the extended sources. Stated errors correspond to the 90 % confidence level. The global metallicity was set to $0.3\,Z_\odot$ for all sources. Fluxes are given in the spectral range $0.4 - 10$ keV, and in units 10^{-14}ergs cm^{-2} s^{-1}. Unabsorbed fluxes are corrected for the fitted N(H). The results correspond to a simultaneous fit of all EPIC spectra, except for the NE source, for which only a pn spectrum was available. Constrained fits are also listed below when the fitted N(H) was outside the 'allowed' range (see Sect. 4.1). Note that solutions with $\chi^2 > 2$ were not included.

Source	Parameters of the *mekal* model					Parameters of the absorbed power law				
	N(H) $(10^{22}$ cm$^{-2})$	kT (keV)	χ^2_ν(dof)	f_X^{abs}	f_X^{unabs}	N(H) $(10^{22}$ cm$^{-2})$	Γ	χ^2_ν(dof)	f_X^{abs}	f_X^{unabs}
N11L	$0.43^{0.46}_{0.40}$	$0.15^{0.16}_{0.15}$	1.63 (162)	23.1	459.					
plume N of N11L	$0.68^{0.73}_{0.64}$	$0.15^{0.18}_{0.14}$	1.29 (175)	11.0	755.	$0.72^{0.92}_{0.57}$	$7.38^{8.76}_{6.37}$	1.79 (175)	11.2	1500.
LH9	$0.41^{0.45}_{0.37}$	$0.18^{0.18}_{0.17}$	1.54 (419)	45.9	663.					
LH10	$0.05^{0.17}_{0.}$	$0.59^{0.66}_{0.52}$	1.39 (35)	4.56	5.56					
NE	$0.36^{0.44}_{0.10}$	$0.22^{0.29}_{0.19}$	1.05 (45)	4.56	34.0					
NW	$0.26^{0.35}_{0.20}$	$0.23^{0.25}_{0.20}$	1.36 (154)	9.29	40.8					
LH9[1]	$0.20^{0.20}_{0.18}$	$0.23^{0.23}_{0.22}$	1.74 (419)	45.0	100.					
LH10[2]	$0.10^{0.18}_{0.10}$	$0.58^{0.63}_{0.51}$	1.41 (35)	4.49	6.51					

[1] N(H) constrained to the interval $0.06 - 0.2 \times 10^{22}$ cm^{-2} (see Sect. 4.1).
[2] N(H) constrained to the interval $0.1 - 0.8 \times 10^{22}$ cm^{-2} (see Sect. 4.1).

4.3, and 4.4, respectively. The last region of diffuse emission, which will be called N11-North, is projected around XMMU J045624.3−662205 (i.e. source # 26), but may not be physically connected to this source. This extended X-ray emission is confined by faint Hα filaments. It is bisected by a north-south oriented ridge of low X-ray surface brightness coincident with an Hα filament; the low X-ray surface brightness is thus probably caused by a higher absorption column density provided by the filament. Meaburn et al. (1989) and Mac Low et al. (1998) studied the kinematics of N11 and revealed the existence of expanding motions in the Hα line at the position of the eastern part of N11-North (hereafter called 'NE', see Fig. 6), while they detected no line splitting further north. The X-ray emission may thus be the result of shocked expanding gas.

Unfortunately, nothing is known on the kinematics of the western part of N11-North (hereafter called 'NW', see Fig. 6).

To study these diffuse X-ray emission regions quantitatively, we have chosen the extraction regions shown in Fig. 6. Nearby source-free regions were used as background for N11L and the extended X-ray emission to its north, but there is no emission-free region near the other sources. Due to fluorescent features in the instrumental background that change with the position on the detector (see e.g. Lumb 2002), we cannot use the background spectrum from a region lying too far away from our diffuse sources for background subtraction. We thus decided to use blank sky event lists provided by Dr Andrew Read (Birmingham University). Since no blank sky files are available for the THICK filter, we have used the event lists associated

with the MEDIUM filter. We note that there is only a slight difference between the THIN and MEDIUM filters in these blank sky files for the regions considered. We also checked that using the MEDIUM blank sky for N11L and the extended X-ray emission to its north gives the same results as with a neighbouring background region. We thus have extracted blank sky spectra over the same detector regions as occupied by the diffuse emissions, then scaled these spectra to correctly subtract the fluorescence lines of the detector (this was only necessary once, for the MOS2 spectrum of LH9). To generate rmf and arf matrices, we used the SAS tasks *rmfgen* and *arfgen* using a detector map of the region to account for the source extension. Note that as these extended emission regions cover generally more than one CCD, the response matrices are still to be taken with caution in SAS v5.4.1. The spectra were then binned to reach a minimum of 20 cts per channel. As we did for point sources, we discarded noisy bins: below 0.4 keV and above 2 keV when the blank sky files were used or above 10 keV for N11L and the extended X-ray emission to its north. We list the parameters of the best-fit models in Table 5. Note that they are consistent with *ROSAT* determinations (Mac Low et al. 1998), but our new results have much smaller error bars.

4.1. Hydrogen Columns

One parameter of the spectral models, the hydrogen column, can be estimated using H I/CO surveys, nebular emission, and stellar photometry. Rohlfs et al.[5] (1984) measured $N(\mathrm{H\,I})$ of $1.8 - 2.4 \times 10^{21}$ cm^{-2} in our *XMM* field-of-view, while Schwering & Israel (1991) quoted 5.6×10^{20} cm^{-2} for the Galactic absorption column. The contribution of H$_2$ can also be estimated using the strength of the ^{12}CO line (Israel et al. 1993) and a conversion factor $N(\mathrm{H_2})/I(^{12}\mathrm{CO})$ of $1.3 - 1.7 \times 10^{20}$ cm^{-2} K^{-1} km^{-1} s. Israel et al. (1993) measured I(^{12}CO) up to 18 K km s^{-1} for N11B and 14 K km s^{-1} for N11C. They also gave values in the range $7 - 21$ K km s^{-1} in the *XMM* field. The minimum absorption column towards N 11 is thus 6×10^{20} cm^{-2}, while the maximum column could reach up to 1×10^{22} cm^{-2}.

E(B−V) measurements (PGMW, Walborn et al. 1999) and Balmer decrements (Caplan & Deharveng 1986, Heydari-Malayeri & Testor 1985, Heydari-Malayeri et al. 1987) provide a second, independent estimate of $N(\mathrm{H})$. With a galactic extinction of $0 - 0.15$ mag towards the LMC (Oestreicher et al. 1995), gas-to-dust ratios of 5.8×10^{21} cm^{-2} mag^{-1} for the Galaxy (Bohlin et al. 1978) and 2.4×10^{22} cm^{-2} mag^{-1} for the LMC (Fitzpatrick 1986), we get the following reasonable estimates of $N(\mathrm{H})$: $0.3 - 2 \times 10^{21}$ cm^{-2} for LH9, $1 - 8 \times 10^{21}$ cm^{-2} for LH10, $0.6 - 6 \times 10^{21}$ cm^{-2} for LH13 or in general $0.3 - 8 \times 10^{21}$ cm^{-2} for sources actually belonging to N11. Combining all the constraints derived in this section, we fitted again the spectra when necessary (see Table 5).

---

[5] Note that Williams et al. (1999) wrongly quoted the value from that paper, but this error did not affect their analysis since they finally used the H I data from a high-resolution ATCA H I survey.
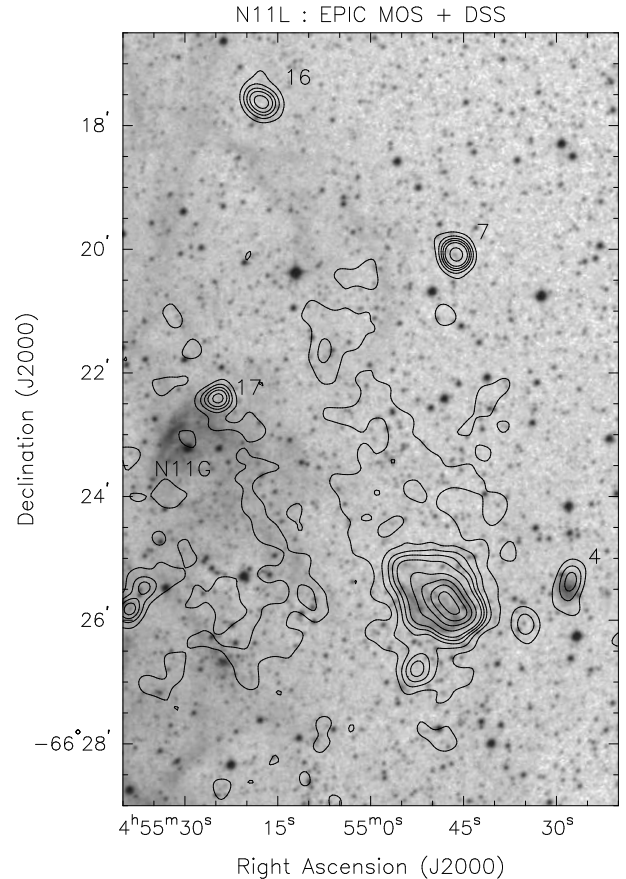

N11L : EPIC MOS + DSS

Fig. 7. Close-up on N11L (DSS+EPIC MOS, as for Fig. 3). Contours have been drawn at levels of 0.35, 0.5, 0.65, 0.8, 1, 1.5, 2, 2.5, and 3 cts pixel^{-2}. Note that a CCD gap ($\sim$10″ in width) is present just east of the SNR. It crosses the field in the NNE-SSW direction, and can be located easily since it corresponds to a region of apparently lower X-ray emission. The X-ray point sources present in the field are labeled.

4.2. The SNR N11L

N11L is an optically faint nebula of diameter $\sim$15 pc at the westernmost part of N 11. It looks like a small filamentary bubble with a northeastern extension. With an age of 10^4 yr, this SNR expands with a mean velocity of $\sim$200 km s^{-1} (Williams et al. 1999). The nonthermal radio emission of N11L is generally coincident with the Hα emission, but additional radio emission appears to the north of the main shell. *ROSAT* observations showed a rather faint X-ray source, compared to other LMC SNRs of similar size. It was cataloged as [SHP2000] LMC 13 or [HP99] 329. In our *XMM-Newton* observations (see Fig. 7), the X-ray emission is revealed in more details. It peaks more or less at the center of the shell, where the Hα (and radio) emission are lower. The X-ray emission is not completely confined to the Hα bubble: some X-ray emission is present just north of that bubble, where radio emission is also enhanced. In addition, we discovered UV emission from N11L in the data from the OM telescope. The UV morphology of the SNR is very similar to the one in the Hα line (see Fig. 8).
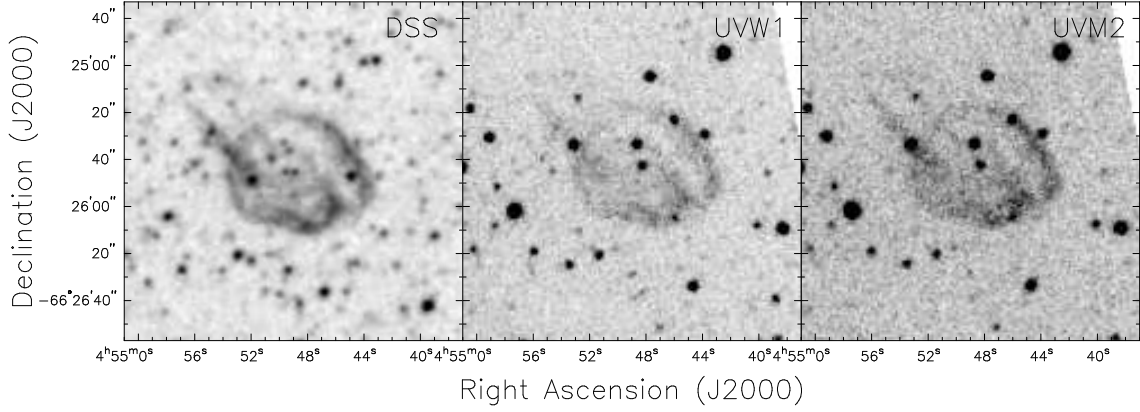
Fig. 8. The SNR N11L at different wavelengths: left, DSS red image; middle, image acquired through the OM UVW1 filter (λ_0=2298 Å and $\Delta(\lambda)$=439 Å) and right, image made in the OM UVM2 filter (λ_0=2905 Å and $\Delta(\lambda)$=620 Å).
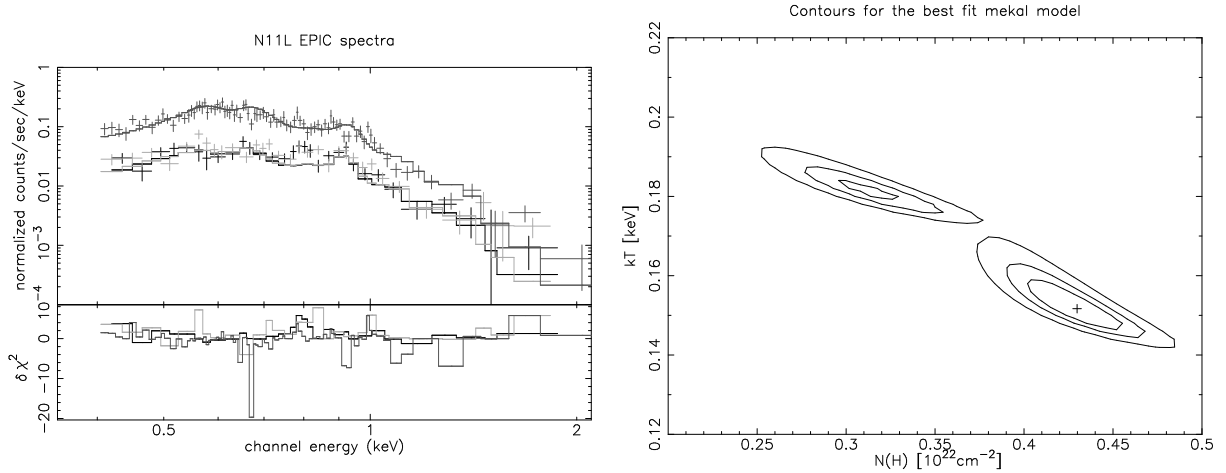

Fig. 9. Left: The X-ray spectrum of N11L, shown along with the best fit absorbed *mekal* model, with N(H) = 0.43×10^{22} cm^{-2} and kT = 0.15 keV (see Table 5). The upper data (dark grey) come from the EPIC pn camera, the lower ones from EPIC MOS (black for MOS1 data and light grey for MOS2). Right: $\Delta\chi^2$ contours for the *mekal* model: contours for 2D confidence levels of 68%, 90% and 99% are drawn. The cross indicates the model used in the fit of the left panel.

The X-ray spectra of N11L are well fitted by a simple absorbed *mekal* model. The parameters from the best fit are given in Table 5, but another solution, with a slightly larger χ^2, also exists, as can be seen in Fig. 9. Note that non-equilibrium models (*nei* or *gnei*) do not give good fits to these data.

The *ROSAT* data suggested the presence of a large 'plume' of diffuse emission extending at least 5′ (or ~70 pc at an LMC distance of 50 kpc) from the nebula. (Williams et al. 1999). This northern extension of diffuse X-ray emission is now clearly detected in the EPIC data of N 11. Compared to N11L, the spectral fit of this X-ray plume shows a similar temperature but a larger extinction. Note that its spectrum can also be fitted by a power-law, but that in this case the exponent Γ is exceptionally large. The physical relationship between N11L and the X-ray plume to its north is not clear. N11L may contribute to some of the hot gas in the plume region, but cannot be responsible for all of it, as the sound-crossing time ($> 5 \times 10^5$yr for c_S ~100 km s^{-1}) of this X-ray plume is much larger than the age of the SNR itself ($\sim 1.5 \times 10^5$yr, Williams et al. 1999).

4.3. LH9

The X-ray emission inside the central shell surrounding LH9 is thought to correspond to hot, shocked gas within a superbubble blown by the cluster stars. The kinematics of this region is complex, with several velocity components along our line-of-sight. However, Rosado et al. (1996) found a general radial expansion velocity of ~45 km s^{-1} for this structure. The X-ray emission peaks near HD 32228 (WC4+OB), where the most violent and complex gas motions are found.

This brightest emission region, roughly 80″ in radius around HD32228, fitted by the model derived for the whole region (see Table 5 and Fig. 10), presents an unabsorbed (i.e. corrected for the fitted N(H)) luminosity of ~ $2 - 12 \times 10^{35}$ erg s^{-1} in the $0.1 - 2$. keV range (*ROSAT* range). In this region, 15 (massive) stars were classified by Walborn et al. (1999) and
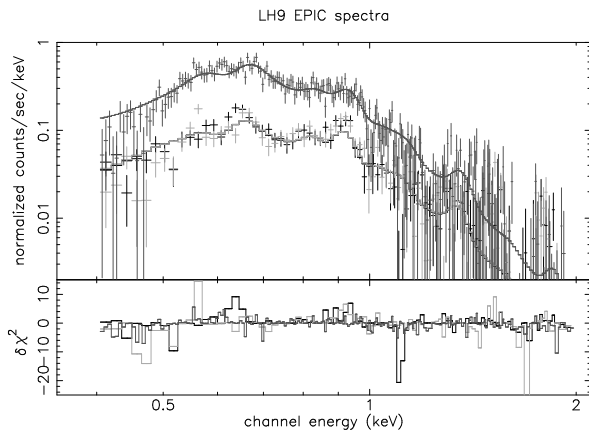
Fig. 10. The X-ray spectrum of the diffuse emission associated with LH9, shown along with the best fit absorbed *mekal* model. EPIC pn data are shown in dark grey, EPIC MOS1 in black and EPIC MOS2 in light grey.

18 others by PGMW[6]. The contribution of the WC4 star to the X-ray flux has been roughly estimated, since the X-ray emission from WC stars is still under debate. Ignace & Oskinova (1999) have found that (binary) WC stars have X-ray luminosities of ~1.4×10^{32} erg s^{-1}. Pollock et al. (1995) measured X-ray luminosities of ~1×10^{32} erg s^{-1} (WR38) or lower for Galactic (binary) WC4 stars, whereas following Oskinova et al. (2003), there has been up to now no conclusive detection of any single WC star. We adopt the highest value as an upper limit. For the other stars, we use $L_X^{unabs}(0.1 - 2.)/L_{BOL}$ empirical relationships (Berghöfer et al. 1997) to estimate their X-ray luminosities from the stellar photometric data published by PGMW and Walborn et al. (1999) and the bolometric corrections provided by Humphreys & McElroy (1984). For the massive star population surrounding HD32228, we then expect a total unabsorbed X-ray luminosity of ~ 1.7×10^{33} erg s^{-1} in the $0.1 - 2.$ keV range. This is at least 100 times lower than observed.

For the whole cluster (i.e. in the same region as the one shown in Fig. 6), the discrepancy is even larger, with a predicted unabsorbed X-ray luminosity of ~3×10^{33} erg s^{-1} in the $0.1 - 2.$ keV energy range, for observations of $8 - 48 \times 10^{35}$ erg s^{-1}. In addition, we have to consider the role of the metallicity of the LMC. A lower metallicity Z implies weaker winds, thus less X-ray emission will be produced, but the absorption by the wind is also lower in this case. Using *ROSAT* data of Galactic O stars, Kudritzki et al. (1996) found that $L_X \propto (\dot{M}/v_\infty)^{-0.38} \times L_{BOL}^{1.34}$, i.e. $L_X \propto Z^{\sim 0.3}$ if we use the dependences of $\dot{M}$ and v_∞ on Z from Vink et al. (2001) and the relationship between $\dot{M}$ and L_{BOL} from Howarth & Prinja (1989). Our predictions of the stellar X-ray luminosity may thus be slightly overestimated, reinforcing the discrepancy with the observations. An additional source of X-ray emission is clearly needed.

---

[6] [W99] 30, 89, 44 (the WC4 star); 62, 21, 84, 50, 41, 51, 68, 61, 72, 36, 87, 75, and PGMW 1052, 1110, 1125, 1160, 1194, 1200, 1239, 1288, 1292, 1303, 1310, 1321, 1342, 1343, 1350, 1357, 1365, 1377

Shocked gas within the superbubble was suggested as the probable cause for this excess X-ray emission. Using the Weaver et al. (1977) model, Dunne et al. (2001) predicted an X-ray emission of ~9×10^{34} erg s^{-1} for the superbubble surrounding LH9. This reduces the discrepancy, but does not solve totally the conflict between observations and theoretical predictions.

With an age of only 3.5 Myr (Walborn et al. 1999), LH9 most probably still contains a lot of Pre-Main Sequence (PMS) stars. With the development of recent X-ray observatories, it is now a common occurrence to serendipitously detect PMS objects in the field of OB clusters (e.g. Rauw et al. 2002, 2003). Actually, the Classical and Weak Line T Tauri stars can present X-ray luminosities up to 10^{31} erg s^{-1}. At the distance of the LMC, these objects would not be resolved as individual sources and could therefore mimic a diffuse emission. Using an IMF slope Γ of −1.6 (PGMW), we find that ~ 10^4 PMS stars of masses in the $0.2 - 2$ M$_\odot$ range might be lurking in the cluster, thus contributing to the X-ray luminosity for a maximum 10^{35} erg s^{-1}.

Another source of X-ray emission may come from a so-called 'cluster wind'. For the Arches cluster, Cantó et al. (2000) have estimated that stars may constitute only 10% of the X-ray emission, the hot intracluster gas being responsible for the rest. A similar process might be at work in LH9, resulting in another increase of the X-ray luminosity. Off-center supernova explosions hitting the swept-up shell and/or colliding wind binaries in the cluster may also provide additional sources of X-ray emission. More observations are needed to determine the importance of these two processes: the presence of these supernovae could be revealed by e.g. observations of high-velocity UV absorptions (Chu & Mac Low 1990) whereas high-resolution spectroscopy of the binaries present in the cluster could enable to find the signatures of colliding winds interactions.

Finally, we may note that soft X-ray emission is also present to the south of LH9 (see Fig. 1). This might indicate hot gas leaking out of the superbubble.

4.4. LH 10

With an age of ~1Myr (Walborn et al. 1999), LH10 is the youngest cluster of N 11. Embedded in the bright nebula N11B, it contains several O3 stars, indicating that even the most massive stars have remained intact and that no SN explosions should have occurred in this cluster yet. In this pristine environment, the stars did not yet have the time to blow a superbubble surrounding the entire cluster. Nevertheless, Nazé et al. (2001) showed that smaller wind-blown bubbles around individual stars or small groups of stars are present, e.g. near PGMW 3209 and around PGMW 3070.

In this field, three X-ray sources have been detected: XMMU J045643.0−662504, 045646.1−662447, and 045648.3−662400 (see Fig. 11). The brightest one corresponds to the area near PGMW 3070 (O6V), a second source is close to PGMW 3120 (O5.5((f*))) and a last one is located to the north of these stars but is without any bright counterpart. Very faint
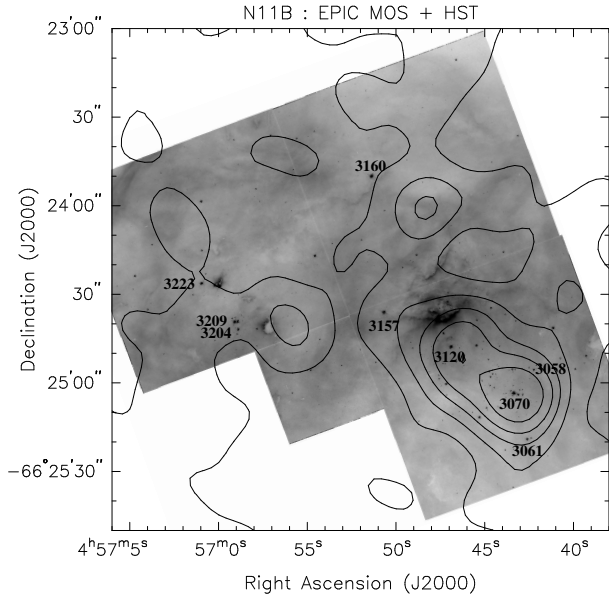
Fig. 11. HST WFPC2 image of N11B (see Nazé et al. 2001) superposed onto X-ray contours (same contours as in Fig. 7). The most important stars are labelled with their PGMW number. Nazé et al. (2001) found expanding regions near PGMW 3204/3209, PGMW 3120, PGMW 3070, and also possibly around PGMW 3160.
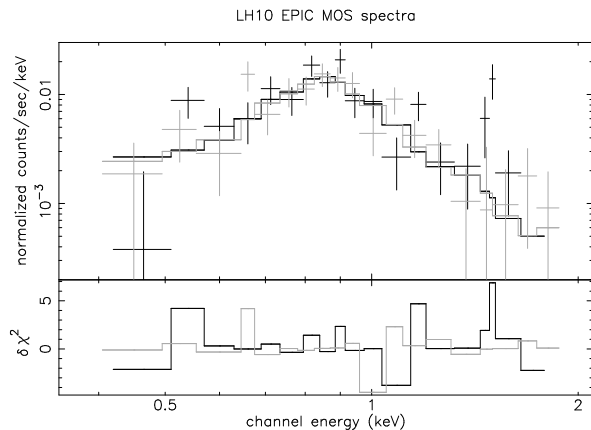

Fig. 12. The X-ray spectrum of the diffuse emission associated with LH10, shown along with the best fit absorbed *mekal* model. EPIC MOS1 are shown in black and EPIC MOS2 in light grey.

diffuse emission is also detected near the optical pair PGMW 3209 (O3III(f*)+OB) and PGMW 3204 (O6-7V). All these correlate well with the positions of wind-blown bubbles found by Nazé et al. (2001). Soft, extended emission is also present all over the cluster (see Fig. 1).

To investigate deeper the origin of these X-ray emissions, we focused on a region of radius 13″ centered on PGMW 3070. Using the models derived for the whole region encompassing LH10 (see Table 5 and Fig. 12), we found that this region possesses an unabsorbed luminosity of $\sim 3.3 - 3.9 \times 10^{33}$ erg s^{-1} in the $0.1 - 2.$ keV range. On the other hand, following the

same procedure as for LH9, we predicted an unabsorbed X-ray luminosity of $\sim 8 \times 10^{32}$ erg s^{-1} for all stars with known spectral types in this small region (PGMW 3058, 3070, 3090, and 3073), i.e. a factor 4 below the observed value. For the whole LH10 (i.e. the same region as that shown in Fig. 6), the emission predicted is 5×10^{33} erg s^{-1}, while the observed value is $\sim 2.2 - 2.6 \times 10^{34}$ erg s^{-1}. The discrepancy is thus similar.

Without doubt, there is a source of X-ray emission in addition to the massive stars themselves. Unlike LH9, hidden SNRs are very unlikely to contribute, since LH10 is much younger and even its most massive stars have not yet evolved. In addition, the youth of LH10 implies that most PMS stars are still in their protostellar stages, where their X-ray emission is strongly attenuated by their parental molecular cloud. However, we note that the X-ray peaks are in regions where bubble expansion and some high-velocity motions have been discovered (Rosado et al. 1996, Nazé et al. 2001): hot shocked gas may thus be an additional source of X-rays. But the peak emission also appears harder than the surrounding soft emissions (see Fig. 1). While there is certainly soft, extended emission in LH10 - maybe associated with shocked winds inside a wind-blown bubble -, this is unlikely the only source of X-rays. A cluster wind and colliding winds in binaries may also be partly responsible for the enhancement of the emission. The contributions of these different sources of X-rays should be disentangled by future X-ray observations, ideally done with a high resolution and a high sensitivity, altogether.

5. LH 13

LH13 is situated to the east of LH9 and LH10. It is embedded in N11C, one of the bright nebular components of N 11, and consists of two compact stellar clusters, Sk −66°41 and HNT, and several field stars. The ages of Sk −66°41 and HNT have been estimated to ≤ 5 Myr and 100 Myr, respectively, suggesting a non-association between the two clusters (Heydari-Malayeri et al. 2000). The same authors proposed that the O stars surrounding Sk −66°41 may have been ejected from the cluster by dynamical interactions.

Two X-ray sources are detected in LH13. The brightest one, XMMU J045744.1−662741 (source # 35) corresponds to Sk −66°41, while a fainter source, XMMU J045749.2−662726 (source # 36), does not seem to have any obvious counterpart (see Fig. 13). The HNT cluster is not detected: this is not totally surprising since the brightest stars in HNT are of spectral type later than A0 and they should thus emit less X-rays (if any). Predicting the X-ray luminosity of Sk −66°41 is not easy, since only its global properties are known: spectral type (O3V ((f*))+OB, Heydari-Malayeri et al. 2000), V magnitude (11.72 mag, Heydari-Malayeri et al. 1987), extinction (E(B−V)=0.11 − 0.22 mag, Caplan & Deharveng 1985, Heydari-Malayeri et al. 1987). Using the same relations as before, we predict an unabsorbed luminosity up to 3×10^{33} erg s^{-1} in the $0.1 - 2.$ keV energy range. This is slightly lower than the observed value $L_X^{unabs} \sim 7.5 \times 10^{33}$ erg s^{-1} for the *mekal* models. The situation here is thus very different from LH9 since no large excess emission is detected. However, we note that the
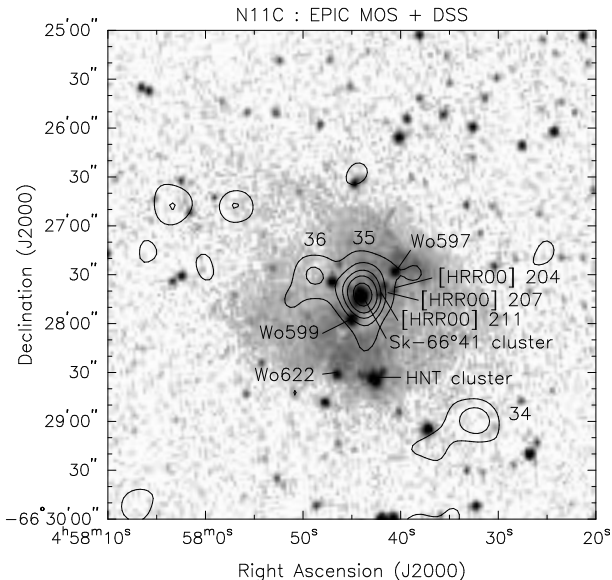
Fig. 13. Close-up on the LH 13 cluster embedded in the N 11C nebula (same contours as in Fig. 7). X-ray point sources present in this field are labeled. The main clusters and early-type stars (Heydari-Malayeri et al. 2000) are also shown.

spectrum[7] of this source is very noisy (see Fig. 14), and that a deeper X-ray observation is needed in order to pinpoint the physical properties of the source. A detailed spectroscopic investigation of the content of the cluster is also crucial to better estimate the expected X-ray emission.

It may seem quite strange that in the dense medium of N 11C, the powerful massive stars in Sk −66°41 have not blown any bubble. The observations of Rosado et al. (1996) do not show any expansion with $v > 10$ km s^{-1} or expanding regions of sizes > 2.2 pc. Using the Weaver et al. (1977) model, a density of 20 cm^{-3} (Heydari-Malayeri et al. 1987) and typical parameters of an O3V star, this lack of detection implies that either the bubble has $R = 37$ pc, corresponding to about 2.5′, and $t = 2.2$ Myr (so that $v = 10$ km s^{-1}) or that the dynamical timescale t is unrealistically short ($t << 1$ Myr) so that the bubble's radius has not reached 1.1 pc yet. Using the former and more realistic physical parameters, we can determine the expected X-ray luminosity of the hypothetical bubble, and we find ~4×10^{35} erg s^{-1} (Chu et al. 1995), which is clearly ruled out by our observations: the modest X-ray luminosity of LH 13 is thus most probably due to the stars of Sk −66°41 alone. However, we may note that the extinction in N 11C is not uniform, and may be rather large in some regions: Heydari-Malayeri et al. (1987) have actually detected extinctions E(B−V) up to 0.9 mag. Extended regions of hot gas with modest X-ray emission might thus be present in N 11C, but the large extinction would prevent us from detecting them in our observation.

---

[7] To avoid contamination from the nearby XMMU J045749.2−662726 (source #36), we had to extract the spectra in a small region some 17″5 in radius. A correction to the encircled energy loss is made via the option *modelee = yes* of the *arfgen* task.
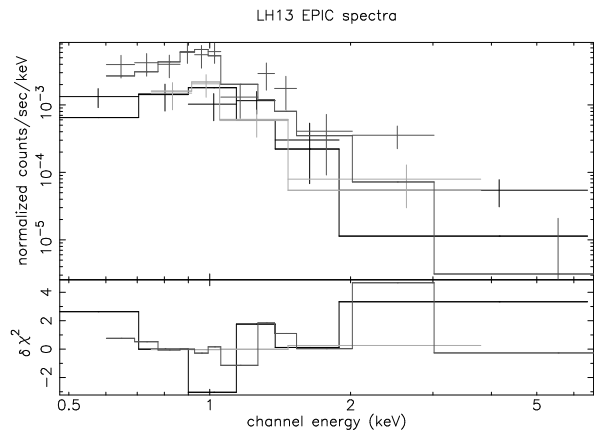

Fig. 14. The X-ray spectrum of source #35, which corresponds to Sk −66°41, shown along with the best fit absorbed *mekal* model. EPIC pn data are shown in dark grey, EPIC MOS1 in black and EPIC MOS2 in light grey.

6. Conclusion

We report in this paper the observations by the *XMM-Newton* satellite of the giant H ɪɪ region N 11 situated in the LMC. In this field, we have detected large areas of soft diffuse X-ray emission and 37 point sources, one of which is apparently associated with a small and poorly known extended object, BSDL 188.

N 11 harbours a wealth of phenomena associated with massive stars: it contains a SNR, N11L, and four OB associations at different stages of evolution and interaction with their surroundings (LH9, LH10, LH13 and LH14). All are detected in the *XMM-Newton* data, except for LH14, which is unfortunately outside of the *XMM-Newton* FOV. The stars from LH9, the largest cluster of N 11, have blown a superbubble which is detected in X-rays as a large soft X-ray emission. It peaks near HD 32228, a dense cluster containing a WR star and several OB stars, and it is rather well confined within the Hα filaments delineating the superbubble. The combined emission of all individual massive stars of LH9 can not explain the high level of emission observed, nor can the contribution from the hot shocked gas of the superbubble as predicted by the Weaver et al. (1977) model. Hidden SNRs, colliding-wind binaries and the often neglected pre-main sequence stars most probably provide additional X-ray emission. It is probably a combination of all these effects that will resolve the discrepancy, since an estimation of the contribution of the latter alone has been shown insufficient to explain the whole X-ray emission. Moreover, we do not exclude that the superbubble is leaking some hot gas since faint, soft emission is detected to the south of the cluster.

The action of LH9 on its surroundings has probably triggered the formation of a second cluster, LH10. The X-ray emission from this younger cluster consists of three rather pointlike sources, in addition to a soft extended emission of reduced intensity. The two brightest sources are not centered on the most powerful stars of the cluster, i.e. the young O3 stars, but seem

associated with the expanding bubbles blown by stars in the SW part of LH10 (Nazé et al. 2001). The total X-ray emission of LH10 is four times larger than the total emission from its stellar components. Since the cluster is still very young, the excess emission can probably not be attributed to hidden SNRs or active T Tauri stars, but it probably originates from the hot gas filling the wind-blown bubbles. To completely understand the X-ray emission from these two clusters, disentangling the individual contributions (extended sources vs. a simple accumulation of non-resolved point sources) is of the utmost importance. However, this is not feasible in a reasonable amount of time with the current X-ray observatories, but N 11 will be a perfect target for the next generation of X-ray satellites.

In contrast, the X-ray emission from LH13 does not show any extended emission and could be well explained by the stars of the Sk −66°41 cluster alone. To the west of the field, the SNR N11L shows hot gas outside the optical bubble, which is associated with an additional radio emission. The spectra of the SNR and of the extended X-ray plume to its north are similar, though with a larger absorbing column for the latter. For the first time, the SNR was also detected in the ultraviolet, and it presents at these wavelengths a morphology very similar to the optical one.

Note that the high excitation blob N11A is not detected in our observation, but this is not completely surprising since at least the theoretically expected X-ray flux from the stellar population embedded in this nebula (Heydari-Malayeri et al. 2001) is very small.

During our X-ray observation, the OM camera onboard *XMM-Newton* has provided unique UV photometry of more than 6000 sources. This photometry is available to the scientific community through CDS.

References

Berghöfer, T.W., Schmitt, J.H.M.M., Danner, R., & Cassinelli, J.P. 1997, A&A, 322, 167

Bica, E.L.D., Schmitt, H.R., Dutra, C.M., & Oliveira, H.L. 1999, AJ, 117, 238

Bohlin, R.C., Savage, B.D., & Drake, J.F. 1978, ApJ, 224, 132

Cantó, J., Raga, A.C., & Rodríguez, L.F. 2000, ApJ, 536, 896

Caplan, J., & Deharveng, L. 1985, A&AS, 62, 63

Caplan, J., & Deharveng, L. 1986, A&A, 155, 297

Chu, Y.-H., & Mac Low, M.-M. 1990, ApJ, 365, 510

Chu, Y.-H., Chang, H.-W., Su, Y.-L., & Mac Low, M.-M. 1995, ApJ, 450, 157

Cohen, R.S., Dame, T.M., Garay, G., Montani, J., Rubio, M., & Thaddeus, P. 1988, ApJ, 331, L95

Dunne, B.C., Points, S.D., & Chu, Y.-H. 2001, ApJS, 136, 119

Evans, N.R., Sasselov, D.D., & Short, C.I. 2002, ApJ, 567, 1121

Fitzpatrick, E.L. 1986, AJ, 92, 1068

Haberl, F., & Pietsch, W. 1999, A&AS, 139, 277 ([HP99])

Henize, K.G. 1956, ApJS, 2, 315

Heydari-Malayeri, M., & Testor, G. 1985, A&A, 144, 98

Heydari-Malayeri, M., Niemela, V.S., & Testor, G. 1987, A&A, 184, 300

Heydari-Malayeri, M., Royer, P., Rauw, G., & Walborn, N.R. 2000, A&A, 361, 877

Heydari-Malayeri, M., Charmandaris, V., Deharveng, L., Rosa, M.R., Schaerer, D., & Zinnecker, H. 2001, A&A, 372, 527

Howarth, I.D., & Prinja, R.K. 1989, ApJS, 69, 527

Humphreys, R.M., & McElroy, D.B. 1984, ApJ, 284, 565

Ignace, R., & Oskinova, L. M. 1999, A&A, 348, L45

Israel, F.P., Johansson, L.E.B., Lequeux, J., et al. 1993, A&A, 276, 25

Kudritzki, R.P., Palsa, R., Feldmeier, A., Puls, J., & Pauldrach, A.W.A. 1996, in 'Röntgenstrahlung from the Universe', eds. Zimmermann, Trümper, & Yorke, MPE Report 263, 9

Jansen, F., Lumb, D., Altieri, B., et al. 2001, A&A, 365, L1

Lawrence, A., Rowan-Robinson, M., Ellis, R.S., et al. 1999, MNRAS, 308, 897

Lucke, P. B., & Hodge, P. W. 1970, AJ, 75, 171

Lumb, D. 2002, 'EPIC background files', XMM-SOC-CAL-TN-0016

Mac Low, M.-M., Chang, T.H., Chu, Y.-H., Points, S.D., Smith, R.C., & Wakker, B.P. 1998, ApJ, 493, 260

Mason, K.O., Breeveld, A., Much, R., et al. 2001, A&A, 365, L36

Meaburn, J., Solomos, N., Laspias, V., & Goudis, C. 1989, A&A, 225, 497

Nazé, Y., Chu, Y.-H., Points, S. D., Danforth, C.W., Rosado, M., & Chen, C.-H. R. 2001, AJ, 122, 921

Oestreicher, M.O., Gochermann, J., & Schmidt-Kaler, T. 1995, A&AS, 112, 495

Oskinova, L.M., Ignace, R., Hamann, W.-R., Pollock, A.M.T., & Brown, J. C. 2003, A&A, 402, 755

Parker, J. W., Garmany, C. D., Massey, P., & Walborn, N. R. 1992, AJ, 103, 1205 (PGMW)

Pollock, A.M.T., Haberl, F., & Corcoran, M.F. 1995, IAUS 163, 512

Rauw, G., Nazé, Y., Gosset, E., et al. 2002, A&A, 395, 499

Rauw, G., De Becker, M., Gosset, E., Pittard, J.M., & Stevens, I.R. 2003, A&A, 407, 925

Rohlfs, K., Kreitschmann, J., Feitzinger, J.V., & Siegman, B.C. 1984, A&A, 137, 343

Rosado, M., Laval, A., Le Coarer, E., et al. 1996, A&A, 308, 588

ROSAT Consortium 2000a, *ROSAT* News 71, "The *ROSAT* Source Catalog of Pointed Observations with the High Resolution Imager (1RXH) (3rd Release)"

ROSAT Consortium 2000b, *ROSAT* News 72, "The Second *ROSAT* Source Catalog of Pointed Observations (2RXP)"

Royer, P., Manfroid, J., Gosset, E., & Vreux, J.-M. 2000, A&AS, 145, 351

Sana, H., Stevens, I.R., Gosset, E., Rauw, G., & Vreux, J.-M. 2004, MNRAS, in press

Sanduleak, N. 1970, Contr. Cerro-Tololo Obs., 89, 1

Sasaki, M., Haberl, F., & Pietsch, W. 2000, A&AS, 143, 391 ([SHP2000])

Schwering, P.B.W., & Israel, F.P. 1991, A&A, 246, 231

Strüder, L., Briel, U., & Dennerl, K. et al. 2001, A&A, 365, L18

Turner, M.J.L., Abbey, A., Arnaud, M., et al. 2001, A&A, 365, L27

Vink, J.S., de Koter, A., & Lamers, H.J.G.L.M. 2001, A&A, 369, 574

Voges, W., Aschenbach, B., Boller, Th., et al. 1999, A&A, 349, 389 (1RXS catalog)

Voges, W., Aschenbach, B., Boller, Th., et al. 2000, *ROSAT* All-Sky Survey Faint source Catalogue (RASS-FSC), Max-Planck-Institut für extraterrestrische Physik, Garching

Walborn, N.R., & Parker, J.W. 1992, ApJ, 399, L87

Walborn, N.R., Drissen, L., Parker, J.W., Saha, A., MacKenty, J.W., & White, R.L. 1999, AJ, 118, 1684

Weaver, R., McCray, R., Castor, J., Shapiro, P., & Moore, R. 1977, ApJ, 218, 377

White, N.E., Giommi, P., & Angelini, L. 2000, The WGACAT version of the *ROSAT* PSPC Catalogue, Rev. 1, Laboratory for High Energy Astrophysics (LHEA/NASA), Greenbelt

Williams, R.M., Chu, Y.-H., Dickel, J.R., Smith, R.C., Milne, D.K., & Winkler, P.F. 1999, ApJ, 514, 798